1-1-2010

Design of functionally graded carbon coatings against contact damage

Rajnish K. Singh
University of New South Wales

Zhifeng Zhou
City University of Hong Kong

Lawrence Kwok Yan Li
City University of Hong Kong

Paul Munroe
University of New South Wales

Mark Hoffman
University of New South Wales

See next page for additional authors

10.1016/j.tsf.2010.05.109

Design of functionally graded carbon coatings against contact damage

Rajnish K Singh[a†], Zhifeng Zhou[b], Lawrence Kwok Yan Li[b]
Paul Munroe[a], Mark Hoffman[a] and Zonghan Xie[a,c]

[a] School of Materials Science and Engineering, University of New South Wales, NSW 2052, Australia

[b] Advanced Coatings Applied Research Laboratory (ACARL)
Department of Manufacturing Engineering and Engineering Management
City University of Hong Kong, Tat Chee Avenue, Kowloon, HKSAR, China

[c] School of Engineering, Edith Cowan University, Joondalup, WA 6027, Australia

Corresponding author: Zonghan Xie, School of Engineering, Edith Cowan University, Joondalup, WA 6027, Australia; Phone: 61 8 6304 5062, Fax: 61 8 6304 5811, email: z.xie@ecu.edu.au

Abstract

Three different functionally graded amorphous carbon (a-C) thin films were deposited on to aluminium substrates using a closed-field unbalanced magnetron sputtering ion plating method. The closed-field configuration prohibits the loss of secondary electrons and consequently enhances the plasma density significantly. The functional gradient of the a-C films was achieved by varying the bias voltage linearly during deposition. Three graded a-C systems possessing different variations in Young's modulus were deposited with the highest Young's modulus at the (i) top surface, (ii) interface or (iii) middle of the film. Of the three systems investigated, the one

[†] Now at Sapphicon Semiconductor Pty Ltd, Sydney Olympic Park, NSW, 2127, Australia

with the highest Young's modulus at the middle of the film thickness was found to exhibit significantly lower levels of cracking at higher indentation depths. Finite element models that included an embedded ring crack controlled by cohesive zone elements were developed to clarify the effect of ring cracks on the deformation of the films. This study provides guidance for the design of functionally graded coatings against contact damage.

1. INTRODUCTION

Carbon-based materials have found applications as tribological coatings in microelectromechanical systems and biomedical devices, primarily due to their chemical inertness, biocompatibility, high hardness and low coefficient of friction. However, there are two major drawbacks that hinder the applications of carbon films: 1) low interfacial toughness due to high intrinsic residual stresses, sometimes up to 10 GPa, which makes the films susceptible to lateral cracks at the interface under contact [1, 2], and 2) low intrinsic coating toughness, normally in the range of 1.8 ~ 2 $MPa.m^{1/2}$ [3,4], which precludes the use of amorphous carbon (a-C) coatings at very high contact pressures.

In order to improve the interfacial toughness, the use of functionally graded carbon coatings has been proposed [5]. These coatings were developed by varying the carbon ion energy during deposition. On one hand, a graphite-like carbon structure formed at the interface with an attendant reduction of residual stress and hence enhanced adhesion; on the other hand, a diamond-like carbon structure formed at the top surface, providing a greater resistance to plastic deformation and wear. However, a recent study on functionally graded materials with a similar

structure revealed that such a gradient design was deleterious to the intrinsic toughness of the coatings [6]. Therefore, it is necessary to improve both the interfacial and intrinsic coating toughness of these carbon coatings if wider applications of these materials are to be achieved.

While the intrinsic coating toughness can be improved by a functionally graded design, as noted earlier [5], there are no reports that both the interfacial and intrinsic toughness of the carbon coatings has been simultaneously improved by the application of such gradient design. In the present work, we focus on how the gradient design can be applied to improve the overall toughness of carbon coating systems. More specifically, three different functionally graded carbon coatings have been developed with unique arrangements of Young's modulus through the coating thickness. The effect of graded Young's modulus within the films upon the deformation and fracture behaviour of these coatings has been analysed with the assistance of depth-sensing indentation and focused ion beam microscopy. Moreover, finite element models were developed based upon these experimental observations, to evaluate the stress distribution in different coating systems and clarify the effect of cracks on their deformation behaviour. Insights have then been gained into the optimal design of functionally graded carbon coatings for contact damage resistance. Also, the discontinuity (pop-in) in the load (P) - displacement (h) curve during loading has been attributed to factors such as the onset of plasticity [7], crack formation [8] and phase transformation [9], depending on the specific material, loading conditions and tip geometry. However it is still unclear which crack type in a brittle coating system corresponds to the formation of pop-ins in the P-h curve. In this study, we investigate the onset of fracture in coatings with a graded Young's modulus.

2. EXPERIMENTAL METHODS

2.1 Film deposition

The amorphous carbon (a-C) films were deposited by closed field unbalanced magnetron sputtering ion plating onto pure aluminium substrates. The substrates were finely polished (Ra ~ 0.03 μm), degreased, ultrasonically cleaned, and subsequently blown dry in flowing nitrogen gas. A computer-controlled commercially available UDP650 magnetron sputtering system (Teer Coatings Ltd, UK) comprising six rectangular cathodes (2 Cr and 4 graphite targets) that operate in unbalanced magnetron mode was used in the experiment. The closed magnetic field coupling results in a high degree of ionization, thus giving intense ion bombardment to the growing films on the substrate surface [10]. The equipment was furnished with a rotating substrate holder with variable rotation speed (0 - 20 rpm) to permit a homogeneous composition of the films. The substrates were biased with pulse DC at a frequency of 250 kHz. The background pressure before deposition was less than 5×10^{-4} Pa. The deposition process of the a-C films comprised four major steps: plasma ion cleaning, adhesive layer, compositionally ramp layer, and pure carbon top layer deposition. The Ar ion etching to the substrate in the first stage was employed to remove contaminants and oxide layers on the substrate surface and thus to guarantee good adhesion. After that, a thin adhesive metal layer (Cr) of about 0.2 μm thickness was prepared, then a Cr/C ramp layer of 0.5 μm thickness (with decreasing sputtering power on Cr targets and increasing sputtering power on C targets) was made for load supporting, and finally the pure carbon films (~2 μm thick) were produced by only sputtering graphite targets with a power of ~2 kW under an Ar gas pressure of 0.2 Pa. The gradual variation of chemical composition in the Cr/C ramp transition layer was beneficial to accommodate stresses and reduce micro-cracking. All the depositions were carried out at ambient temperature. During deposition, the substrates

were not heated. However, the ion bombardment to the substrate increased its temperature, which was estimated to be lower than 200°C. The deposition rate for the pure a-C coatings was about 0.66 μm/hour. The relative low deposition rate resulted from the low sputtering yield of graphite materials. Because the a-C coatings (top layer) contain only one element (i.e., carbon), there is no the so-called multilayer effect, therefore, the influence of substrate rotation speed on the composition and structure of the resulting films was insignificant. In this experiment, a rotation speed of 5 rpm was used for all depositions. The total thickness of the films was in the range of 2.5 – 3 μm.

It has been reported that the sputtered non-hydrogenated carbon films possess an amorphous microstructure and have a wide range of hardness, density, tribological performance [12,13]. Their mechanical properties could be varied in a controllable and repeatable manner by selecting appropriate deposition parameters such as bias voltage, which determines mainly the energy of ions bombarding on the growing film surface. In the present study, three functionally graded amorphous carbon (a-C) films were designed and fabricated on pure aluminium substrates (purity > 99.99 at.%) by varying the bias voltage linearly between -40 and -140 V during the final deposition stage of pure carbon. The deposition conditions for the Cr adhesive layer and Cr/C ramp layer remained the same. The first coating system, i.e., a-C12 (Figure 1 a), was processed by gradually varying the bias voltage from -40 to -140 V during deposition in an attempt to produce a gradient in Young's modulus (E) from the interface (lower E) to the top surface (higher E). The second coating system (a-C21) was deposited inversely to a-C12 in an attempt to produce a reverse gradient in Young's modulus from the interface to the surface (Figure 1 b). The third coating system (a-C121) was deposited by varying the bias voltage form -

40 to -140 V for deposition of the first half of the coating thickness (~ 1 μm thick) and then from -140 to -40 V for the second half (Figure 1 c) . In such a case, a unique gradient in Young's modulus was created in this system with the highest Young's Modulus value located at half of the coating thickness and the lowest Young's modulus residing both at the top surface and the interface. For all the three systems, the pure carbon coating thickness was kept constant at ~2 μm. Hard coatings of higher stiffness and hardness are commonly used to protect ductile substrates in technical applications. This means that ideally, the Young's modulus and hardness of the substrate material used in the model system should be lower than 125 GPa and 20 GPa (corresponding to that of a-C coatings prepared at -40 V), respectively. Consequently, unalloyed Al was selected as the substrate, since it possesses a Young's modulus of 77 GPa, a yield strength of 0.120 GPa and a hardening modulus of 4 GPa [13]. Finally, six monolithic carbon coatings with a thickness of 2 μm were deposited on Si (100) substrates at constant bias voltages of -40, -60, -80, -100, -120 and -140 V respectively to clarify the correlation between the bias voltage and the Young's modulus.

2.2 Nanoindentation

To obtain a relationship between deposition bias voltage and Young's modulus of the coating, a nanoindenter (TriboIndenter, Hysitron, Inc) with a Berkovich tip was used. At a constant load peak of 8 mN, 20 indentations were performed on each of the a-Cs deposited at bias voltages of -40, -60, -80, -100, -120 and -140 V on Si (100) substrates. The 'multiple-point unload method' developed by Oliver and Pharr was used for determining Young's modulus and hardness [14] in which the Poisson's ratio of the a-C films is assumed to be 0.25; loading and unloading times were kept constant, 10 seconds for each, and the tip was held for 5 seconds at the peak load. The

maximum depth of penetration for the most compliant coating deposited with bias voltage -40 V was 190 ± 5 nm, i.e., less than 10% of the film thickness. Therefore, the effect of Si substrate may be neglected in determining the mechanical properties of the coatings deposited at various bias voltages [15, 16]. To introduce fracture damage in the graded films on aluminium substrates, a UMIS Nanoindenter (CSIRO, Australia) equipped with a spherical-tipped indenter of 5 μm radius was used at peak loads of 75, 100, 125, and 150 mN. Loading and unloading were performed using load control with load applied in 100 steps with a 0.1 second hold following each increment.

2.3 Subsurface damage observation

Subsurface damage of the films on the aluminium substrate was analysed using a dual-beam focused ion beam (FIB) workstation (FEI Nova 200 Nanolab, FEI company, USA). The method has been outlined in detail elsewhere [1]. Briefly, a protective layer of platinum (1 μm thick) was initially deposited onto the coating surface in the vicinity of the indent, and then cross-sections of the indented region were milled by the ion beam, using beam currents of 7000 pA for the initial cuts and 3000 pA for the final cleaning mills. Subsequently, the region was imaged by the electron beam operated at 5 keV.

2.4 Finite element modelling

The establishment of design guidelines of gradient coating systems against contact damage requires a deeper understanding of the mechanisms by which deformation and fracture occur in each particular system. To that end, an axisymmetric finite element model (FEM) (Figure 2) was

developed using ANSYS 11 (ANSYS Inc, Canonsburg PA, USA). The general assumptions and parameters have been reported in an earlier study [1]. In the present work, the thickness of the film (t) and the radius of the indenter (R) were assumed to be 3 μm and 5 μm, respectively. The aluminium substrate was modelled assuming bikinematic hardening with a Youngs modulus of 77 MPa, yield stress of 120 MPa and hardening modulus of 4 GPa. The a-C films were hard and assumed to behave in a purely elastic manner during indentation. The variation of Young's modulus across the film thickness was modelled by utilising the temperature-dependent Young's modulus feature in ANSYS and constantly varying the temperature within the film. For the simplicity, residual stress was not considered [1, 17-19] and set constant at zero by applying a thermal expansion coefficient of zero. According to a previous study, a 200% increase in residual compressive stress in the coating would only result in a 6% increase in the maximum radial stress at the asymmetric axis at the coating/ substrate interface [1]. Nevertheless, due to the complex nature of graded coating structures, it is difficult to estimate variation of residual stress across the thickness of the coatings. In order to analyse the effect of cracking on deformation behaviour of the coated systems, a straight crack at a distance of 3 μm from the axisymmetric axis was embedded from the top surface to the half of the coating thickness to simulate the ring crack. In addition, a crack parallel to the interface is inserted, starting at the lower end of the previously embedded vertical ring crack, to simulate the spalling of the coating after the formation of the ring crack. The ANSYS contact element CONTA171 was used with a special feature of debonding, coupled with the TARGE169 element, to simulate the fracture process by means of cohesive zone modelling (CZM). The input parameters were maximum normal stress (σ_{max}), tangential stress (τ_{max}) and their corresponding characteristic gap distances at completion of debonding $\left(u_n^c, u_t^c\right)$ calibrated to correspond with expected fracture energy. The intrinsic

fracture energy for the occurrence of a ring crack in both normal and shear cracking was assumed to be the same, 30 J/m^2 [3,4]. The maximum stresses (σ_{max}, τ_{max}) were assumed to be 4 GPa and the gap distances in both normal and tangential directions following debonding were 0.015 μm, assuming elastic fracture energy is given as $\frac{1}{2}\sigma_{\max}u_n^c$ [20]. To overcome convergence difficulties due to debonding, artificial damping of 10^{-5} second was used.

3. RESULTS AND DISCUSSION

3.1 Nanoindentation

The values of Young's modulus were doubled when the deposition bias voltage increased from -40 V to -140 V (Figure 3). The observed trend, i.e. Young's modulus increasing with the bias voltage, is in agreement with an earlier finding [21]. The identification and quantification of the Young's modulus – bias voltage relation was used for the subsequent design of different graded carbon coatings.

The load (P) – displacement (h) curves for all the three coatings corresponding to maximum loads of 100, 125 and 150 mN are shown in Figure 4. The compliance of the coated systems is observed to follow the order of a-C12, a-C121 and a-C21 with a-C12 showing greatest resistance to elastic contact deformation. For the indentation using maximum load of 100 mN, a pop-in is observed at a load of ~92 mN in the coating a-C12 (Figure 4 a). However, no pop-in is observed in either a-C21 or a-C121. Increasing the contact load to 125 mN renders further pop-ins in the a-C12 and the first pop-in in the a-C21 coating at a load of ~110 mN (Figure 4 b). In contrast, no pop-in is observed in the a-C121 coating, suggesting a better resistance to cracking than a-C21

and a-C12. On a further increase of the load to 150 mN, a-C121 eventually yielded a pop-in the *P-h* curve (Figure 4 c). It is worth noting that, in all the cases investigated here, the step size of the pop-ins is greater than that observed in our earlier studies of nanoindentation of diamond-like carbon (DLC) thin films on ductile substrates [1, 4]. Moreover, the step size in the a-C21 and a-C121coatings is smaller than in the a-C12.

The cross-sectional images of indents made upon the different coating systems, corresponding to maximum loads of 100 mN, 125 mN and 150 mN are shown in Figure 5 (a-g). Structural discontinuities or cavities can be seen at the interface between the substrate and the bonding/buffer layer. This condition has been observed for all coating systems, even prior to any indentation (Figure 6), and hence was not due to indentation damage. According to a recent report that carbon coatings deposited on hardened steel substrates showed better adhesion properties than carbon coatings deposited on non-hardened steel substrates [22], the poor adhesion may be attributed to the low load-bearing capability of the soft aluminium substrates.

For indentations corresponding to maximum load of 100 mN, three type of cracks, i.e., ring, radial and lateral cracks are present in a-C21 and a-C12 (Figure 5 a & b). However, no ring crack is identified in a-C121 (Figure 5 c). Compared to a-C12 and a-C21, the development of radial cracks is restricted in a-C121. For a-C12, delamination occurred only at the interface of the bonding layer and the coating, whereas for a-C21 the delamination was observed at both the interface of the bonding layer and the substrate and the interface of the bonding layer and the coating for a-C21 (Figure 5 b). In coating a-C121, delamination occurred solely at the interface of the bonding layer and the substrate (Figure 5 c). Figure 7 shows views of the indentation

surface following indentation up to 100 mN. A concentric ring crack was observed in the case of the coating a-C12 (Figure 7 a), which was otherwise not observed in the case of coatings a-C21 and a-C121 (Figure 7 b & c). Interestingly unlike a-C12, the asperities under the indent area were deformed relative to asperities outside of the indentation area as in the cases of the a-C21 and a-C121 coatings, consistent with the complaint surface layer expected from a lower deposition bias voltage [23].

When the maximum load was increased to 125 mN, cracks developed further in all three coating systems (Figure 5 d-f). Most critically, only minor ring cracks were present in a-C121 (Figure 5 f) and corresponding *P-h* curve (Figure 4 b) does not exhibit a pop-in. The occurrence of 'major' ring cracks was observed to occur in a-C121 on a further increase of the load to 150 mN (Figure 5 g) and correlate well with the pop-in events in their corresponding *P-h* curves (Figure 4 c). Hence, the pop-in in the *P-h* curves may be used to monitor occurrences of major ring crack. In comparison, it is difficult to detect the occurrence of radial cracks from the *P-h* curves (Figure 5 c & f). This may be explained as follows: a) the growth of the radial crack may be relatively discreet, compared with the ring crack, and the resultant energy release rate may be too small for the crack to be detected in *P-h* curve as a pop-in which reflects a high energy release rate. Instead it will alter the slope of the *P-h* loading curve; b) in spite of radial crack formation, the indenter is partially supported by the surrounding film and membrane stresses [21]. Therefore, the loss of the film stiffness due to the occurrence of the radial crack is a gradual process whereas formation of major ring crack is unstable resulting in a sudden change in film stiffness and a *P-h* pop-in.

3.2 Finite element analysis

Radial stress in the a-C films is responsible for the formation of radial cracks that were observed to initiate at the interface between the film and the substrate directly below the indenter. Radial stress distribution within the three coating systems studied at a normalised depth (*h/t*) of 0.5 is shown in Figure 8. It can be seen that the magnitude of the tensile stress at the interface is lower (15 GPa) in a-C12 than for a-C21 (22 GPa), due to lower elastic modulus at the interfaces; 125 GPa versus 250 GPa. For the a-C12 and C121 systems, the tensile stresses have similar values at the interfaces (15 GPa). But in a-C121, unlike a-C12 and a-C21, the maximum tensile stress is observed in the middle of the coating, which diminishes gradually and also broadly in the radial direction outside of the area of contact of the indenter **(**Figure 8 c). In both of the coatings a-C12 and a-C121 and unlike a-C21, the tensile radial stress was distributed broadly in the radial direction across the interface. Whereas in a-C121, the tensile stress is mostly confined in the middle of the coating as a result of increasing modulus in that region. This means the maximum stress is not located near a surface where a potentially larger defect population is more likely to initiate fracture.

Radial cracks were observed in a-C21 and a-C121 at 100 mN (Figure 5 b & c). According to the distribution of radial stress in both coatings, a-C21 would form a radial crack before a-C121 (Figure 8 b & c). We also examined the crack formation in a-C12 and a-C121 following low load indentation to 75 mN. Radial cracks were observed in a-C121, but not in a-C12 at 75 mN (Figure 9). This can be explained as follows: though the same radial stress can be observed at same contact depth in a-C12 and a-C121 near to the axisymmetry axis, the depth of penetration is

different in a-C12 and a-C121 at a constant force. a-C12 has stiffer surface on a relatively compliant subsurface, whereas a-C121 has the reverse configuration. So at constant force, i.e. at 75 mN, a-C121 will undergo more bending or depth (see inset of Figure 10), and hence increased radial stress to facilitate the formation of a radial crack. It is also interesting to see the formation of ring crack in a-C12 can suppress the radial stress at the interface (Table I).

On evaluating the radial stress at the top surface, a-C12 showed the highest stress followed by a-C121 and then a-C21, which is consistent with the findings of Suresh et al. [24]. The ring crack was vertical relative to the interface in a-C12, whereas an inclined acute ring crack was present in a-C21 and a-C121. For a-C12, the top surface is stiffer than the material underneath. This gradient arrangement could provide a greater driving force for ring crack formation and may cause a sudden advancement of the crack in the material (Figure 5 a) [24]. For a-C21 and a-C121, however, the lower modulus at the top surface would generate lower tensile stresses. This is also in agreement with the general finding in functionally graded materials that the crack resistance is greater if the crack is present in the relatively more compliant side [19, 25]. This may explain why there is no observation of ring crack in a-C121 at a load of 100 mN.

Under normal contact conditions, plastic deformation occurs in contacting materials when the contact pressure is greater than the hardness of the materials. Consequently, the higher the hardness, the higher the pressure required to yield the graded carbon coatings. The plastic deformation of the asperities on the top surface of the a-C21 coatings will be greater than the cases of a-C12 and a-C121 due to the relatively high hardness value (25 GPa) of the surface of a-

C12. These less deformed asperities will then also act as a stress concentration centre, and hence will assist the formation of the ring cracks [18].

The effect of ring crack propagation upon the predicted normalised load (P/R^2) and displacement (h/t) curves for the a-C12, a-C21 and a-C121 systems is shown in Figure 10. (Note that the model calculations were undertaken under displacement control and hence pop-ins cannot be observed, unlike the experiments which were undertaken under load control.) For reference purposes, a plot corresponding to a-C21 without a ring crack has been included. It is worthwhile to note that no appreciable difference was observed in simulated P-h curves for different coating systems, when modelled without any crack, for depths more than 10% of coating thickness [26]. In the simulated *P-h* curves with a ring crack, the a-C12 showed more load bearing capacity below the normalised depth of 0.08 followed by a-C121 and then by a-C21 (inset Figure 10). These behaviours demonstrated in the simulated *P-h* curves were similar to the experimentally recorded *P-h* curves in Figure 4, before the observation of a pop-in. But, above a normalised depth of 0.08, a-C12 exhibited a gradual decrease in slope in the corresponding *P-h* curve (inset Figure 10). Examination of the deformed model for a-C12, shows that the decrease in the slope in *P-h* correlates well with the simulated initiation of debonding of the cohesive zone element at the surface. Also at this depth range, indenter penetration into the coating was quite small, so the influence of the substrate can be neglected. Similar to the experimental observations, the coatings a-C21 and a-C121 experienced less resistant force than a-C12 at corresponding depths before the formation of the first ring crack (Figure 4 a & b). At an intermediate normalised depth of 0.25, an apparent change in slope was observed in the a-C12, as complete separation in the cohesive zone element occurred. A similar event was observed in a-C21, but at a relatively larger depth (0.28). The change in the slope was correlated with the formation of the ring crack,

according to the model. The phenomenon of precipitous change (pop-in) in the slope corresponds to the complete formation of the ring crack and subsequently spallation of the coating in their respective models (marked as pop-in in Figure 10). This is consistent with experimental observations in regard to the order in which the pop-ins were observed. Therefore, we conclude that the pop-ins most likely result from the spalling of the coating material following the formation of the ring crack rather than from the initiation of the crack (such as Figure 5 b & f). Similar observations have been made in our previous study of a DLC film on steel substrate, in which we observed the ring crack, but no pop-in; when spalling resulted upon further loading, the pop-in was consequently observed [1]. In modelling we have not included a radial crack, but experimentally it was observed to form first in both the a-C21 and a-C121 coatings. Hence, the FEM might have underestimated the compliance of a-C21 and a-C121 at higher depths.

According to Abdul-Baqi et al. [17], shear and axial stresses influence delamination during loading and unloading, respectively, and initiate delamination outside and beneath the indenter's contact area, respectively. From the FIB cross sectioning, delamination is only observed beneath the indenter area, indicating that delamination predominately occurs during unloading due to axial stresses only and, therefore, shear stresses were not considered further. It is noticeable in Figure 5 a, d & e that whenever delamination was observed at the interface of the coating and the interlayer, there were observations of both ring and radial cracks. In Figure 5 b, c & f where delamination was observed at the interface of the substrate and the interlayer, a radial crack was observed. Observations of ring and radial cracking together during loading correspond to fracture of the coating in any case. This leads to a significant loss of compliance of the coating and, hence, the suppression of axial stress during unloading. This will not be the case, if any one of

these cracks occur alone. This explanation was further confirmed at 150 mN on a-C121 which showed delamination above the interface as a ring crack and radial crack were observed (Figure 5 g).

4. CONCLUSIONS

We have designed and then processed various graded a-C films of tailored Young's modulus by varying the deposition bias voltage. Experiments showed that a graded coating (a-C121) in which the relatively high Young's modulus is obtained at half of the coating thickness provided better contact damage protection under higher indentation depth than coating systems with relatively higher stiffness at either the upper or interfacial surface. We did observe, however, radial cracking in a-C121 at an early stage of loading; this is believed to be due to defects at the interface, which can be potentially reduced by improved substrate surface preparation. We also demonstrated by both experiment and FEM that spalling of the coating after the formation of a ring crack is related to a pop-in recorded on the *P-h* indentation curve. We also explained how ring crack formation affects the formation of other cracks in the system and that the occurrence of delamination location at interfaces depends on the formation of ring and radial cracks.

Acknowledgement:

The authors acknowledge the Australian Research Council (ARC) for funding the research under DP0451423 - Development of Deformation-Mechanism Based Parameters for Improved Design of Hard Coatings - and the Department of Education and Science and Technology (DEST), Australia, for providing an International Postgraduate Research Scholarship (RKS).

References:

[1] R.K. Singh, M.T. Tilbrook, Z.H.. Xie, A. Bendavid, P.J. Martin, P.R. Munroe, M. Hoffman, J. Mater. Res. 23(1) (2008) 27.

[2] E. Liu, L. Li, B. Blanpain, J.P. Celis, J. Appl. Phys. 98 (2005) 073515

[3] J.S. Wang, Y. Sugimura, A.G. Evans, W.K. Tredway, Thin Solid Films 325 (1998) 163.

[4] Z.H. Xie, R. Singh, A. Bendavid, P.J. Martin, P.R. Munroe, M. Hoffman, Thin Solid Films 515 (2007) 3196.

[5] S .Zhang, X.L. Bui, Y. Fu, Thin Solid Films 467(1-2) (2004) 261.

[6] S. Suresh, Science 292 (2001) 2447.

[7] D.F. Bahr, D. E .Wilson, D. A. Crowson, J. Mater. Res. 14 (1999) 2269.

[8] X. Li, D. Diao, B. Bhushan, Acta Mater. 45 (1997) 4453.

[9] J.E. Bradby, J.S. Williams, J. Wong-Leung, M.V. Swain, P. Munroe, J. Mater. Res. 16 (2001) 1500.

[10] S. Yang, D. Camino, A.H.S. Jones, D.G. Teer, Surf. Coat. Technol. 124 (2000) 110.

[11] S. Yang, D.G. Teer, Surf. Coat. Technol. 131 (2000) 412.

[12] S. Yang, X. Li, N.M. Renevier, D.G. Teer, Surf. Coat. Technol. 142 (2001) 85.

[13] H. Pelletier, Tribol. Int. 39 (2006) 593.

[14] W.C. Oliver, G.M. Pharr, J. Mater. Res. 7 (1992) 1564.

[15] B. Bhushan, X. Li, Int. Mater. Rev. 48 (2003) 125.

[16] A.C. Fischer-Cripps, Nanoindentation, Springer, New York NY, 2002.

[17] A. Abdul-Baqi, E. Van der Giessen, Thin Solid Films 38 (2001) 143.

[18] K. Komvopoulos, Z.Q. Gong, Int. J. Solids Struct. 44 (2007) 2109.

[19] M.T. Tilbrook, L. Rutgers, R.J. Moon, M. Hoffman, Int. J. Fatigue 29 (2007) 158.

[20] G. Alfano, M.A. Crisfield,.Int. J. Numer. Meth. Eng. 50 (2001) 1701.

[21] K.Y. Li, Z.F. Zhou, C.Y. Chan, I. Bello, C.S. Lee, S.T. Lee, Diamond Relat. Mater. 10 (2001) 1855.

[22] K.H. Lau, K.Y. Li, Tribol. Int. 39 (2006) 115.

[23] R.K. Singh, Z.H. Xie, A.Bendavid, P.J. Martin, P.R. Munroe, M. Hoffman, Diamond Relat. Mater. 17 (2008) 975.

[24] S. Suresh, A.E. Giannakopoulos, J. Alcala, Acta Mater. 45 (1997) 1307.

[25] X.F. Yao, W. .Xu, H.Y. Yeh, Polym. Test. 26 (2007) 122.

[26] V. Linss, N. Schwarzer, T. Chudoba, M. Karniychuk, F. Richter, Surf Coat. Technol. 196 (2005) 287.

Captions

Figure 1 Schematic illustration of variation of Young's modulus with coating thickness in the coating systems (a) C12, (b) C21, and (c) C121.

Figure 2 Finite element model configurations for simulation of indentation of a-C coatings on aluminium

Figure 3 Variation of Young's modulus of a-C coatings deposited at different bias voltages.

Figure 4 Variation of the indentation load, *P*, versus depth, *h*, curves for nanoindentation tests conducted on gradient a-C coatings a-C12, a-C21 and a-C121 deposited on aluminium at maximum loads of (a) 100 mN (b) 125 mN and c) 150 mN. A spherical tipped indenter of 5 μm in radius was used.

Figure 5 Secondary electron images of cross-sections of graded a-C coatings on aluminium substrates following nanoindentation to: (a-c) 100 mN, (d-f) 125 mN and (g) 150 mN. Ring, radial and lateral cracks are observed, with increasing levels of apparent damage under increasing loads. Less subsurface damage is observed for the a-C121 coating.

Figure 6 Secondary electron image of cross-section of a-C121 coatings on aluminium showing pre-existing cavities at the interface.

Figure 7 Secondary electron images of top surfaces of graded a-C coatings (a) a-C12, (b) a-C21 and (c) a-C121mN following indentation at 100 mN using a spherical-tipped indenter of 5 μm in

radius..

Figure 8 Distribution of radial stress (σ_{rr}) in different a-C coating systems: (a) a-C12, (b) a-C21, and (c) a-C121 at normalised indentation depth (*h/t*) of 0.5.

Figure 9 Secondary electron images of cross-sections of gradient a-C coatings on aluminium substrates following nanoindentation to 75 mN on (a) a-C12 and (b) a-C121.

Figure 10 Simulated normalised load, P/R^2, vs depth, *h/t*, loading curves for all the three coating systems a-C12, a-C21 and a-C121 containing a ring crack. A change in slope can be observed in the curve corresponding to a pop-in in experiments results. For reference, a curve of a-C12 has been included with no ring crack in the model.

Table

Table I Values of normalised radial stress ($\sigma_{rr}/\sigma_y \times 10$) at the a-C film and substrate interface with normalised depth (h/t) during loading with and without ring crack.

Table I

Table I. Values of normalised radial stress ($\sigma_{rr}/\sigma_y \times 10$) at the a-C film and substrate interface with normalised depth (h/t) during loading with and without ring crack.

h/t	a-C12 (σ_{rr}/σ_y)		a-C21(σ_{rr}/σ_y)		a-C121(σ_{rr}/σ_y)	
	Without crack	With crack	Without crack	With crack	Without crack	With crack
0.10	3.36	3.37	4.69	4.68	3.26	3.26
0.20	12.35	10.35	17.53	15.16	11.96	10.35
0.50	14.67	12.09	20.80	17.74	14.19	12.10

Figure 1

Click here to download Figures (if any): Figure 1.pptx

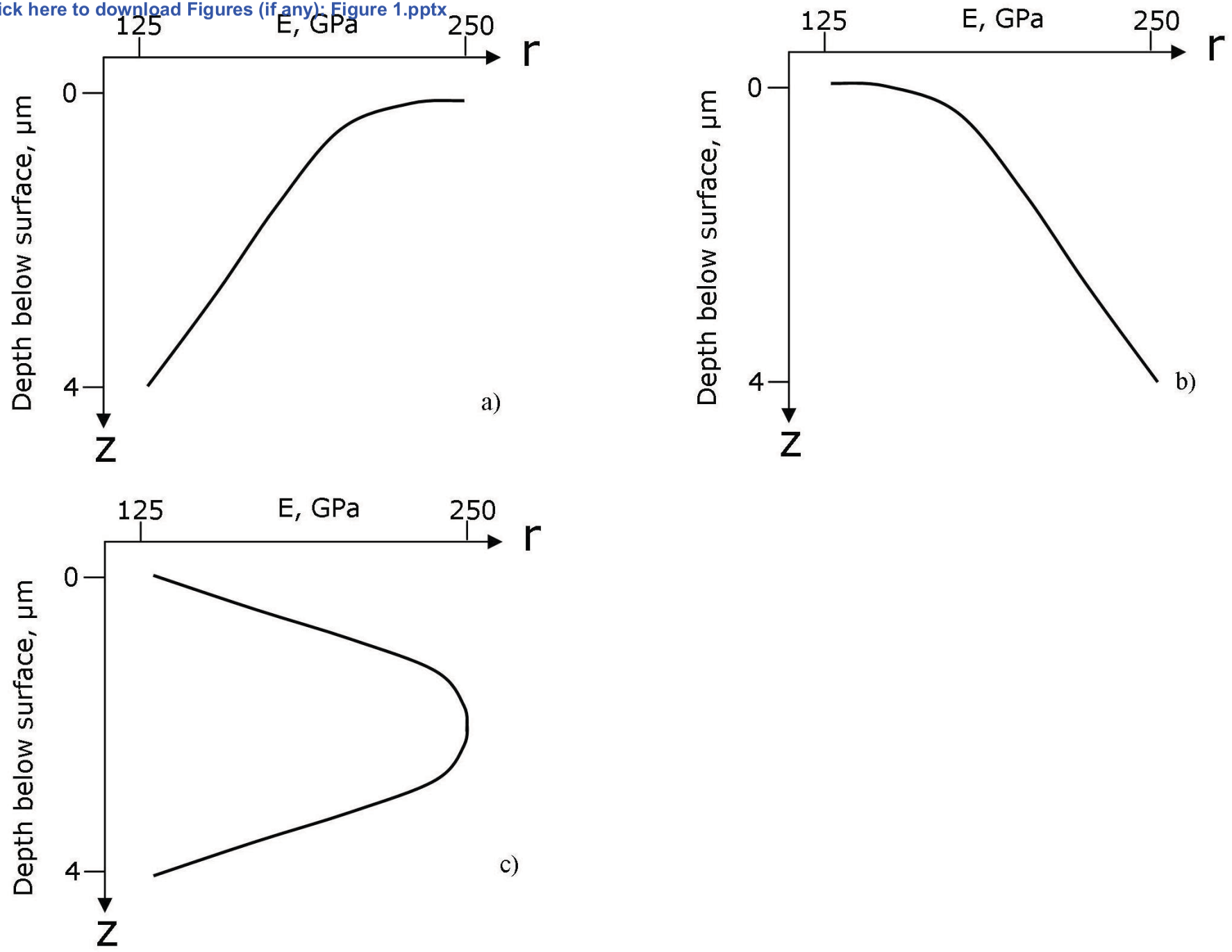

Figure 2
Click here to download Figures (if any): Figure 2.pdf

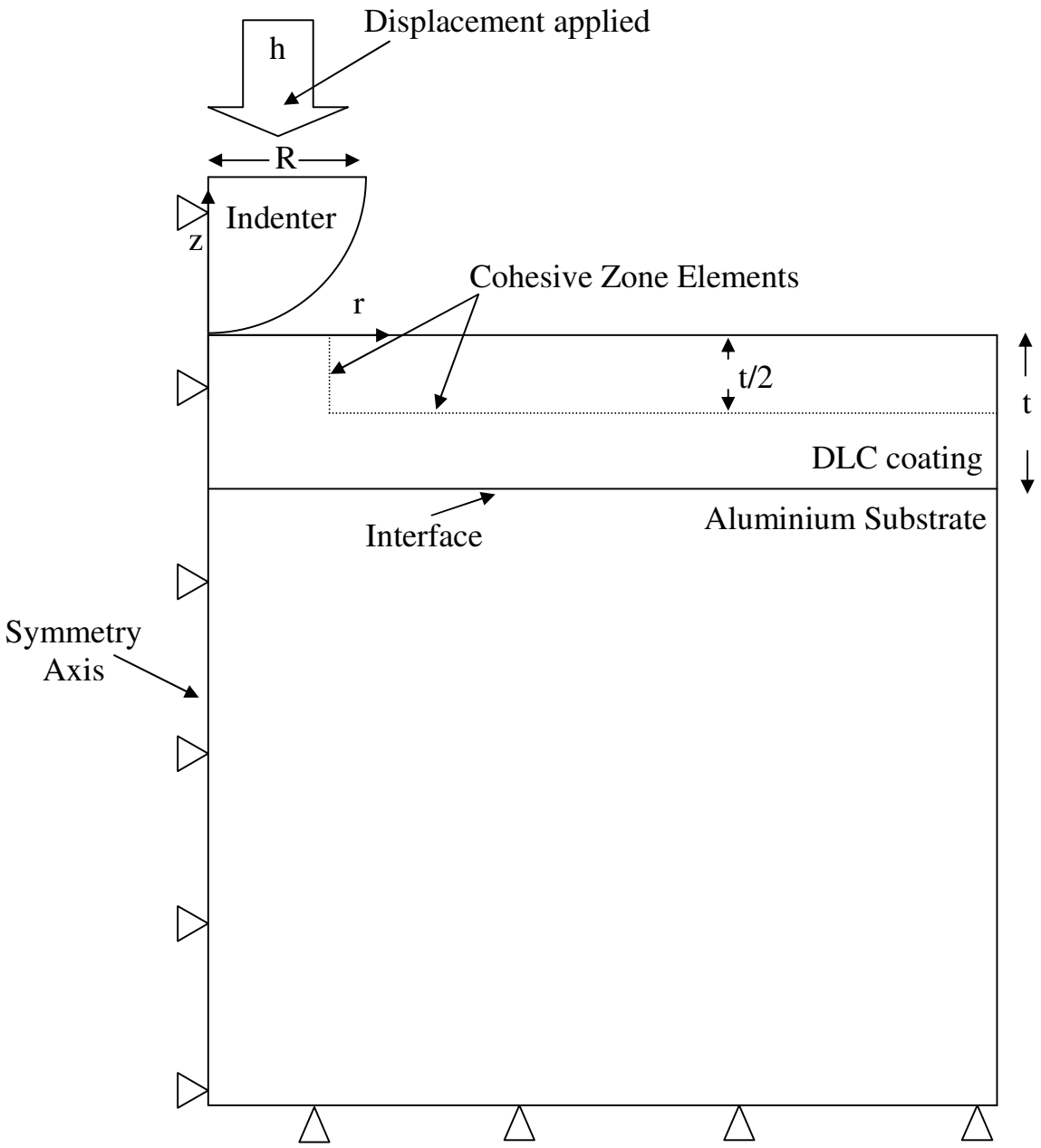

Figure 3
Click here to download Figures (if any): Figure 3.pptx

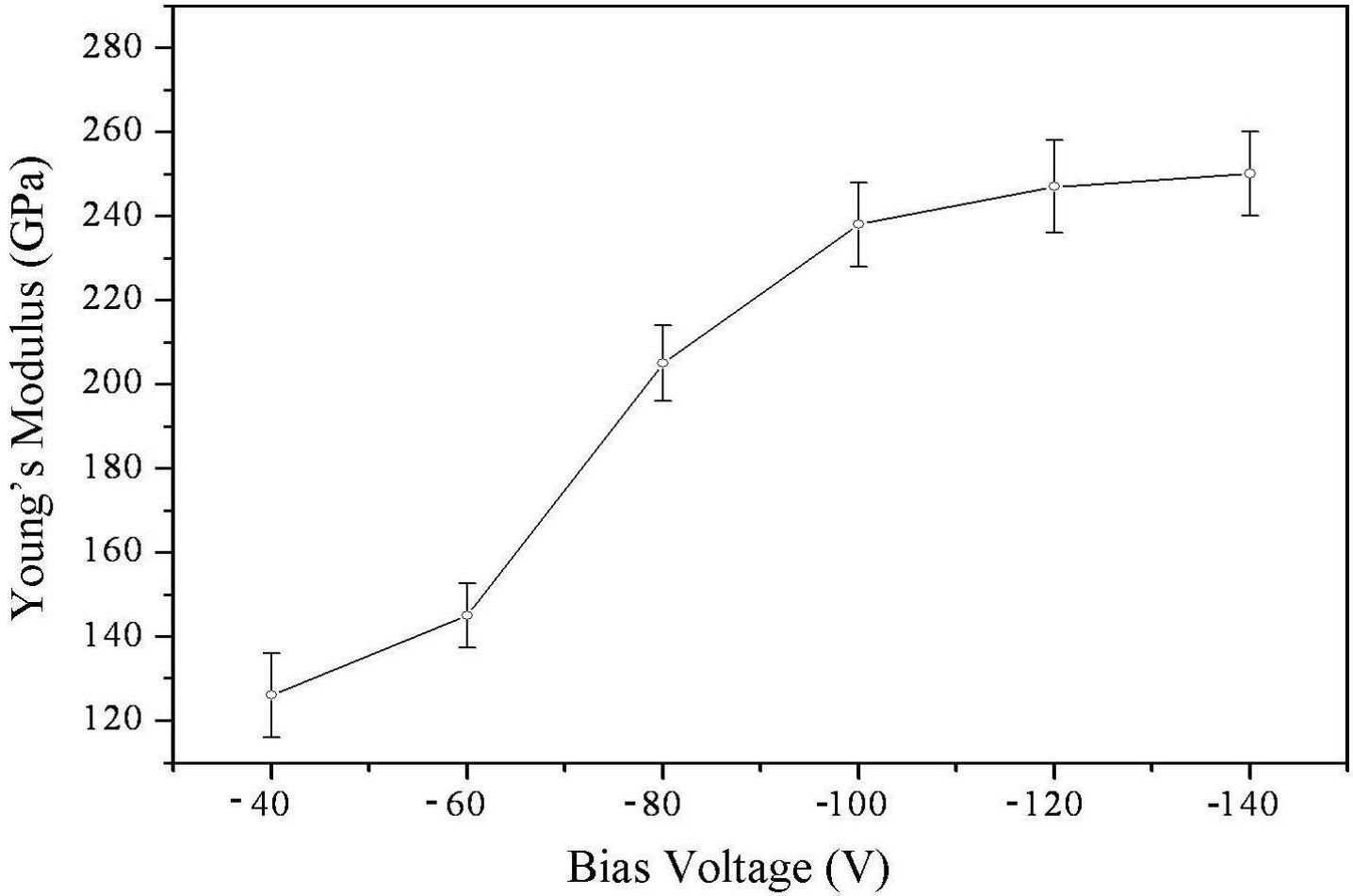

Figure 4a
Click here to download Figures (if any): Figure 4a.pptx

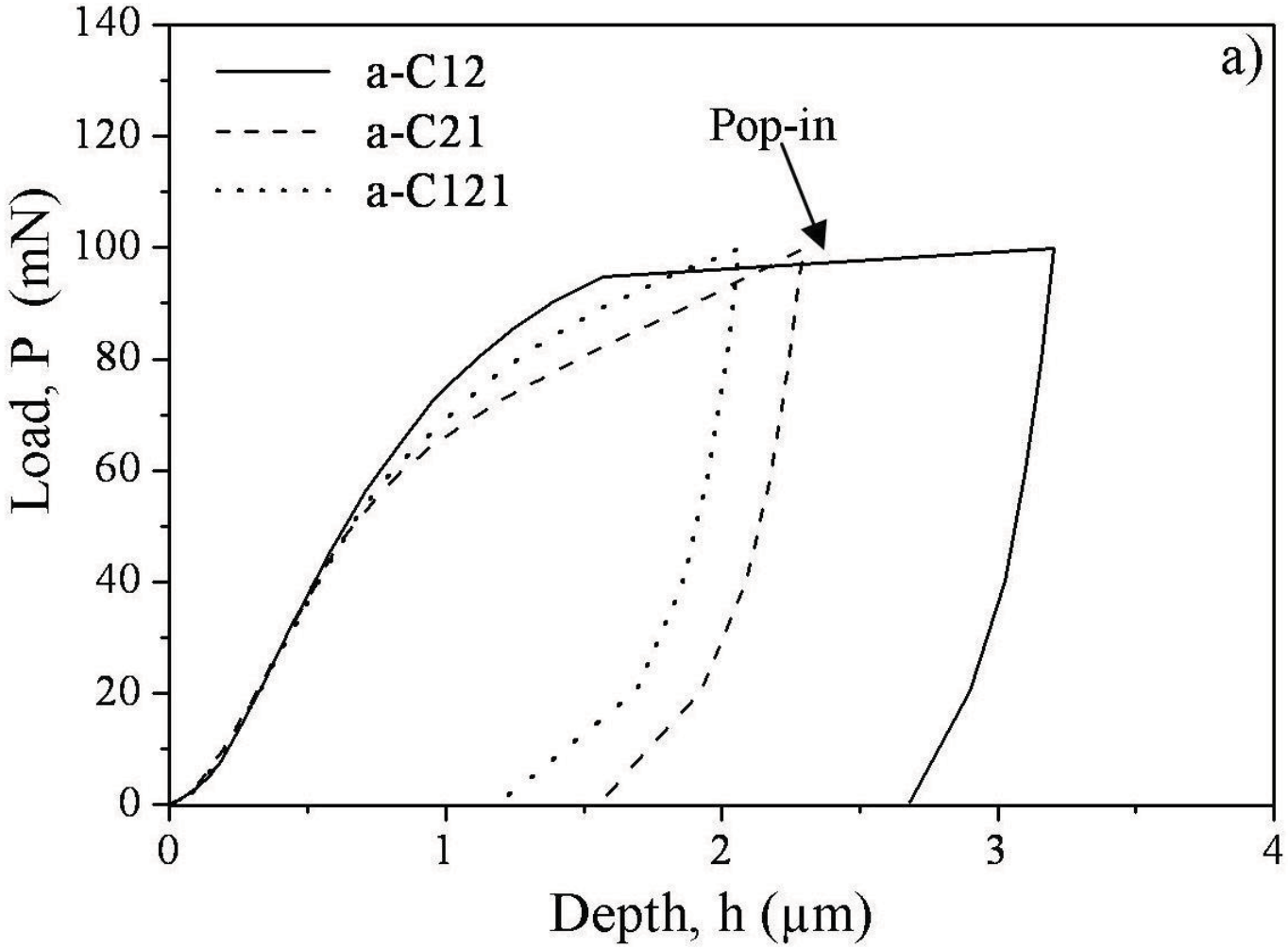

Figure 4b
Click here to download Figures (if any): Figure 4b.pptx

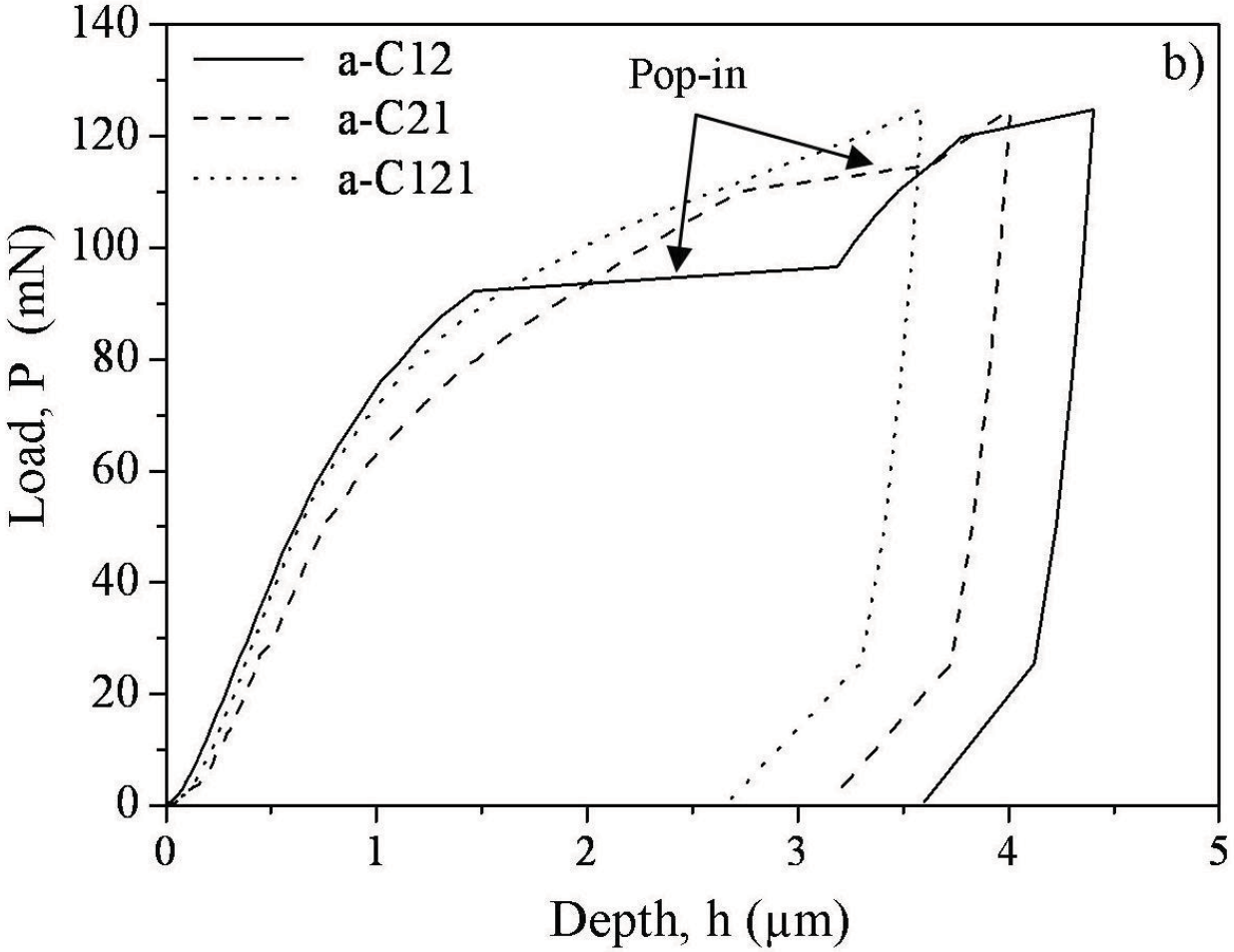

Figure 4c
Click here to download Figures (if any): Figure 4c.pptx

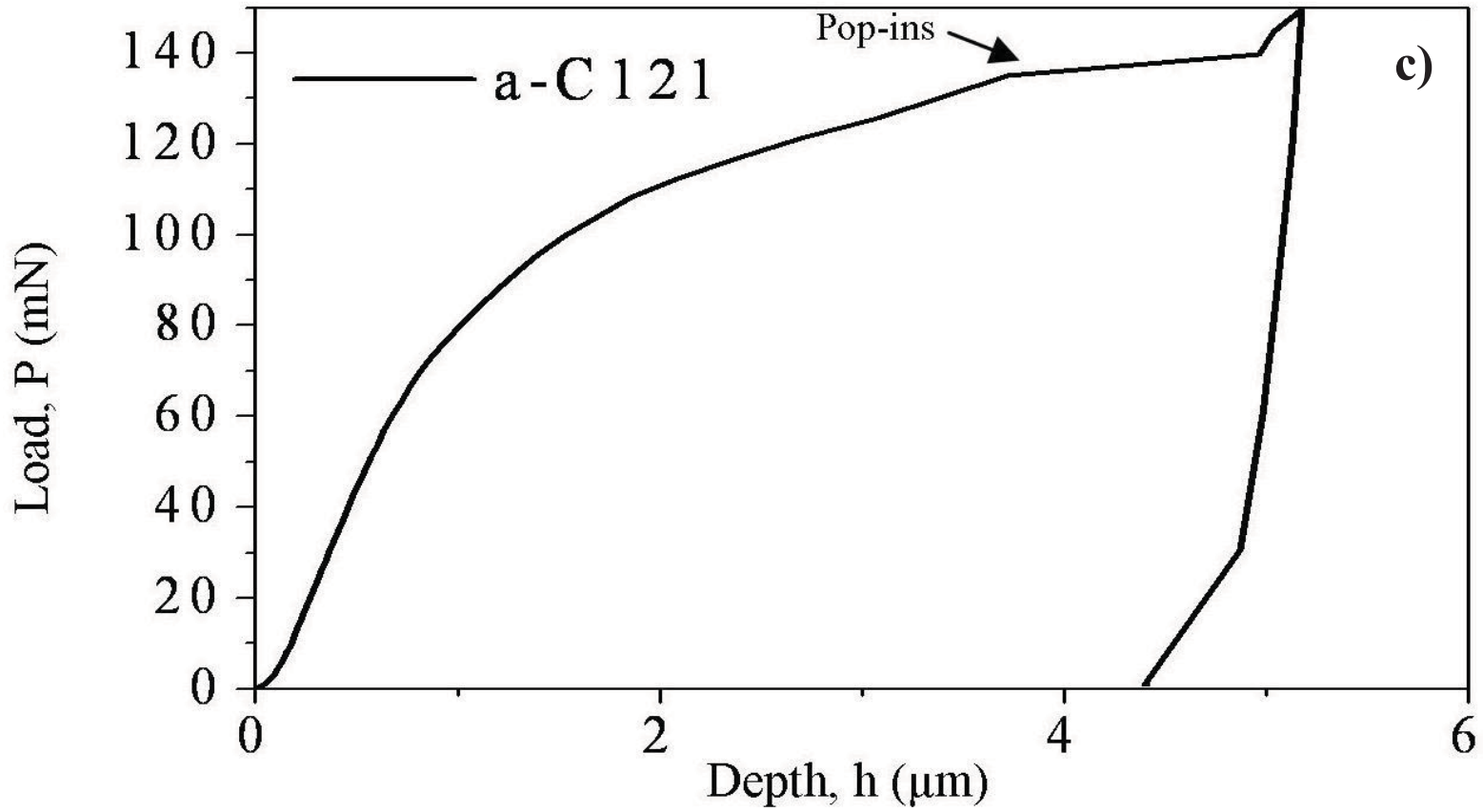

Figure 5 a-f

Click here to download Figures (if any): Figure 5 a-f.pptx

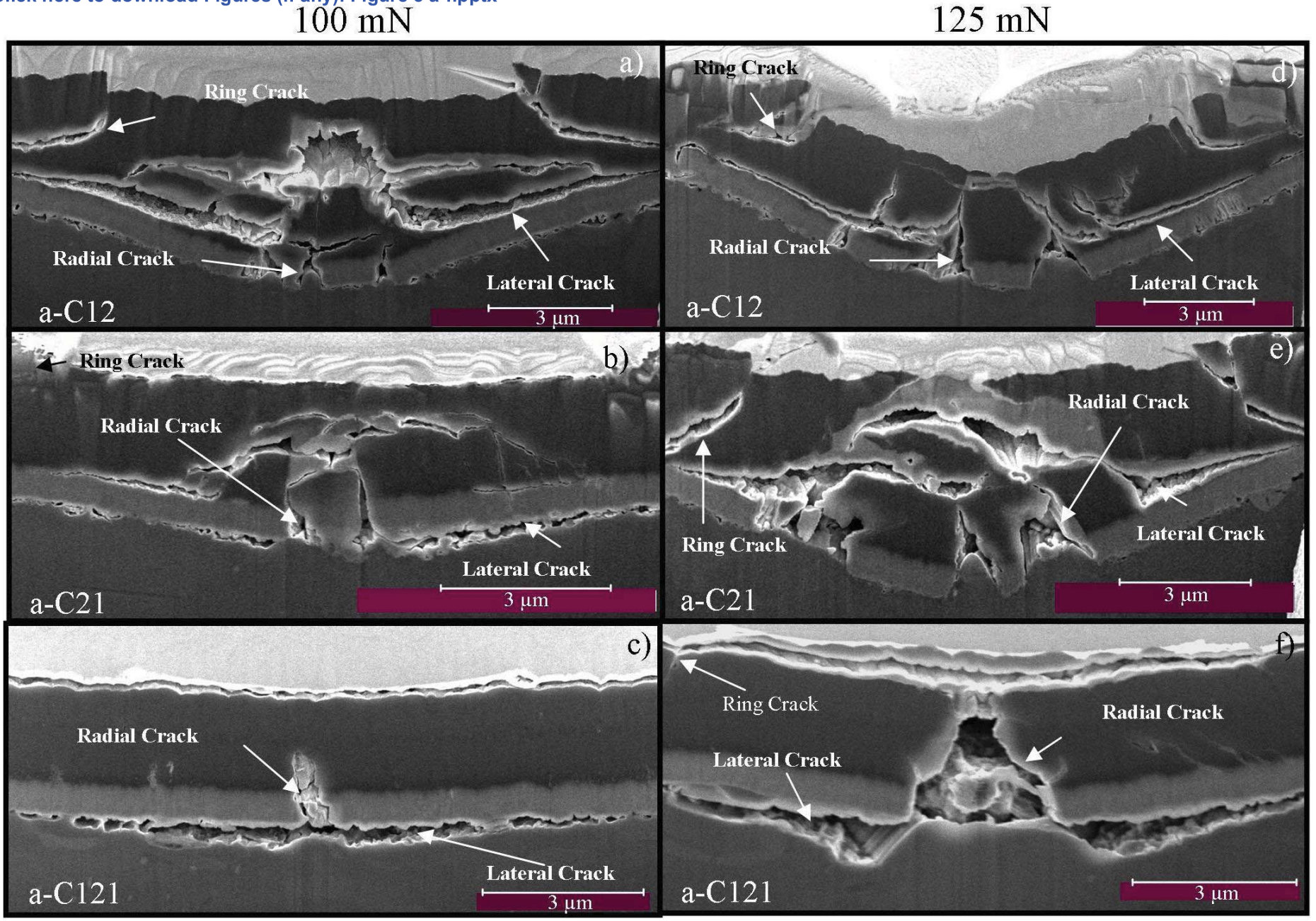

Figure 5g
Click here to download Figures (if any): Figure 5g.pptx

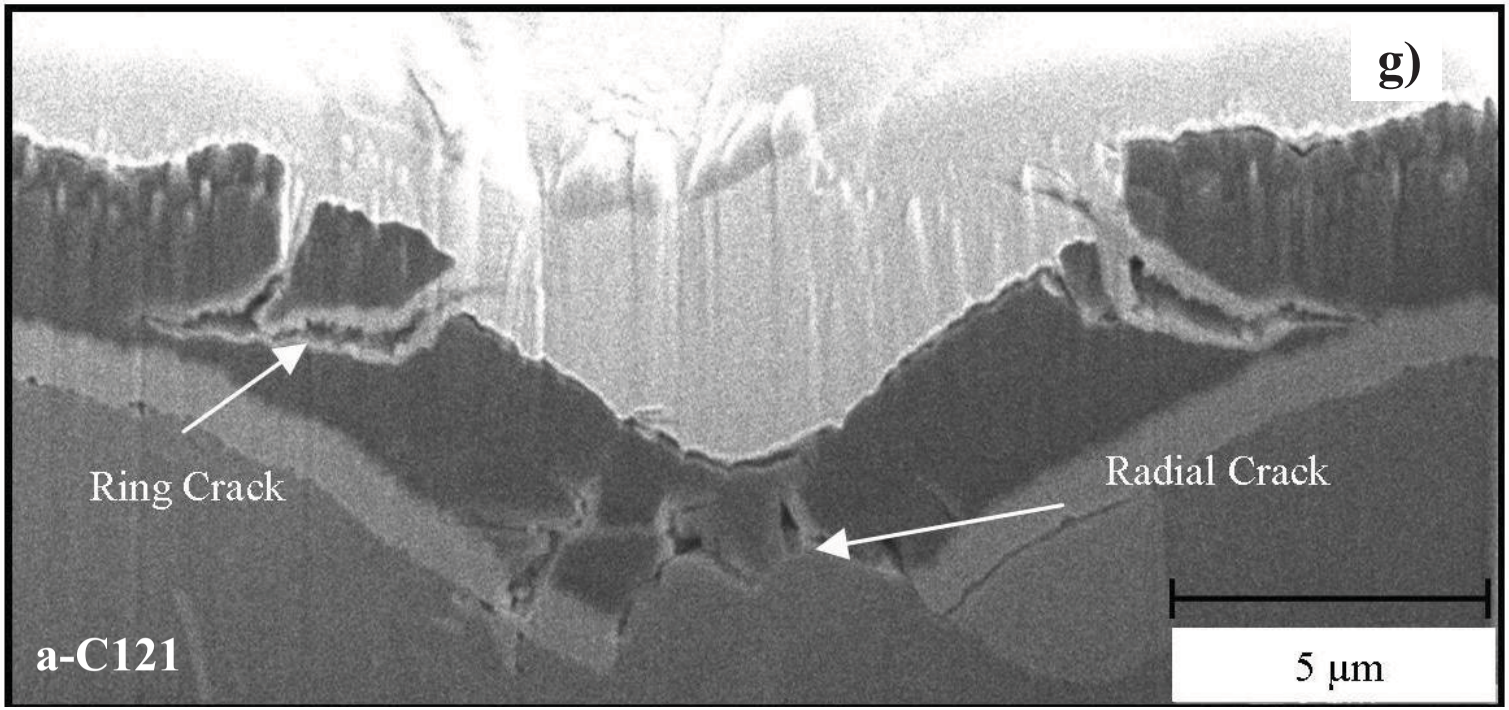

Figure 6
Click here to download Figures (if any): Figure 6.pptx

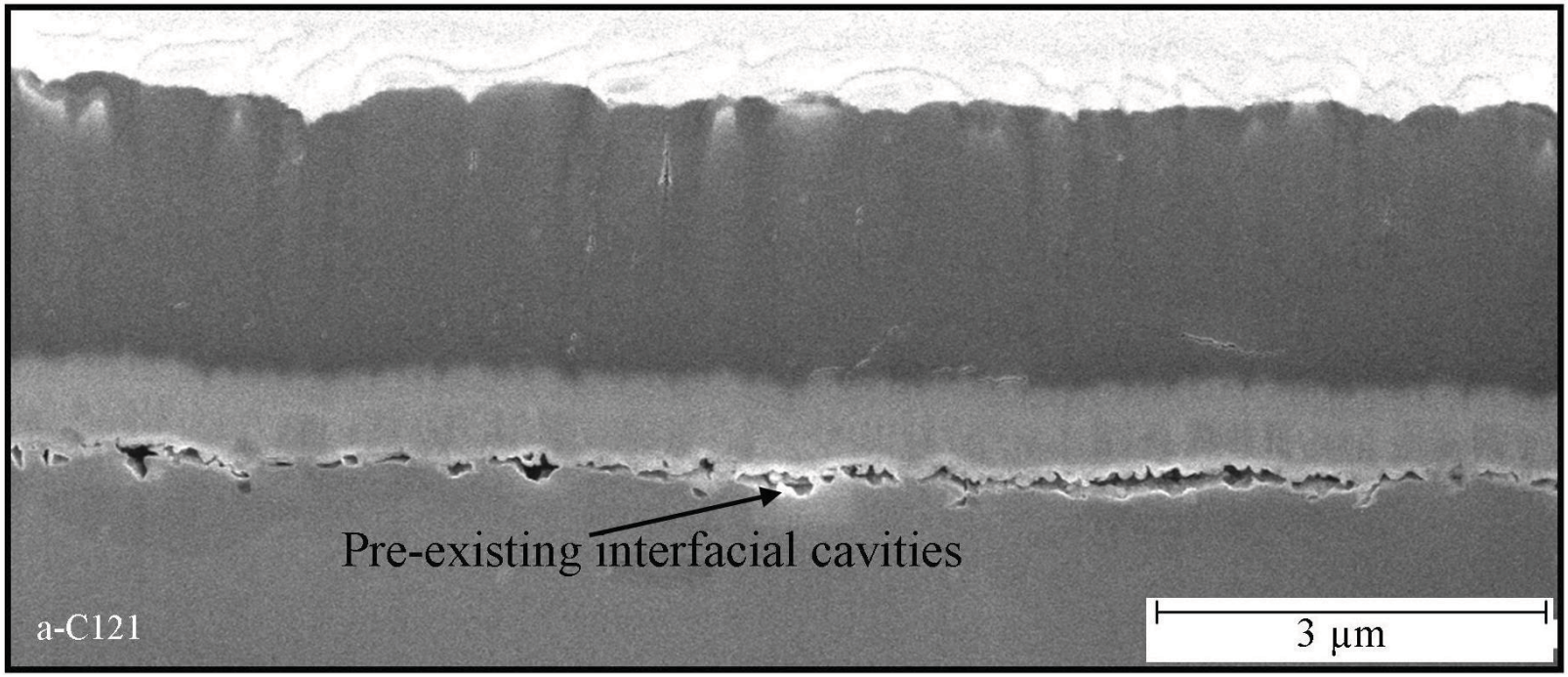

Figure 7

Click here to download Figures (if any): Figure 7.pptx

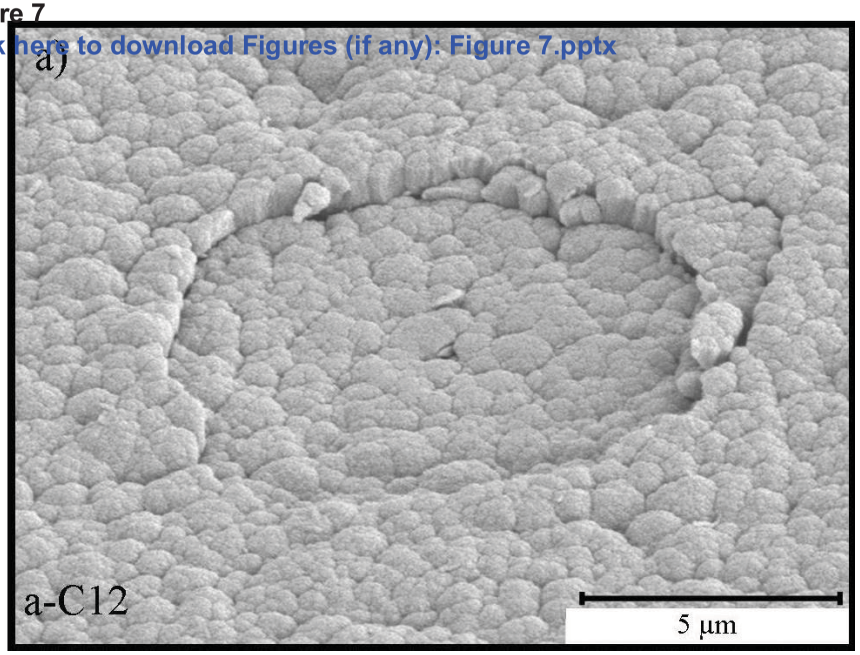

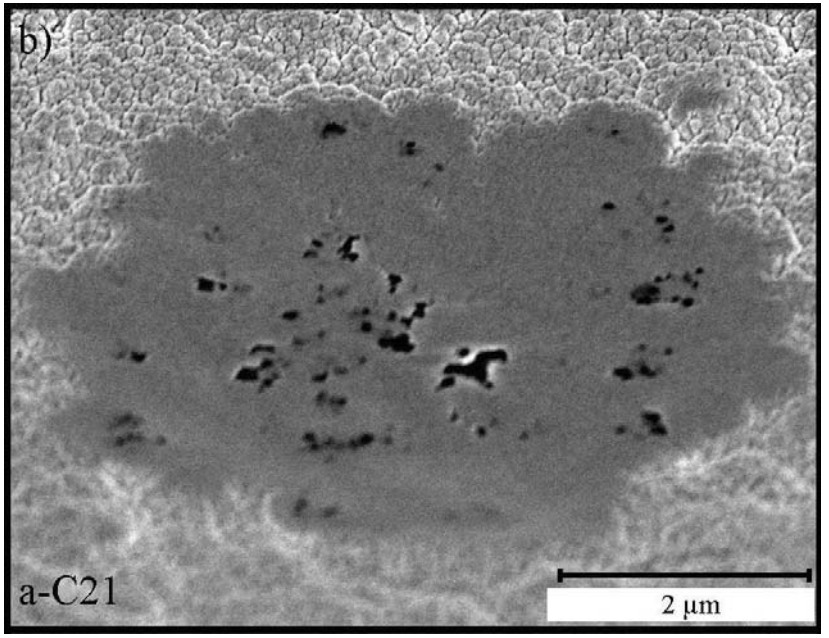

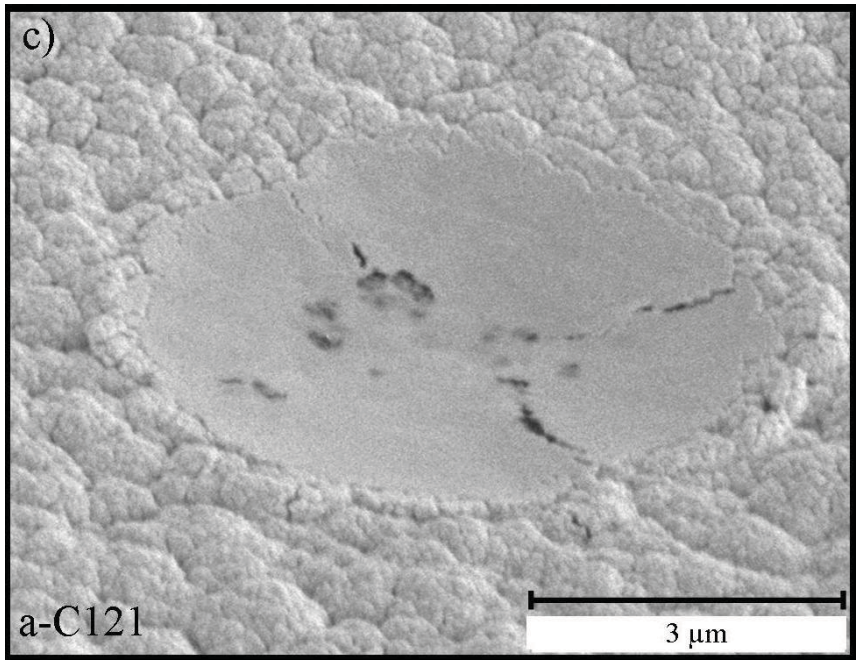

Figure 8
Click here to download Figures (if any): Figure 8.pptx

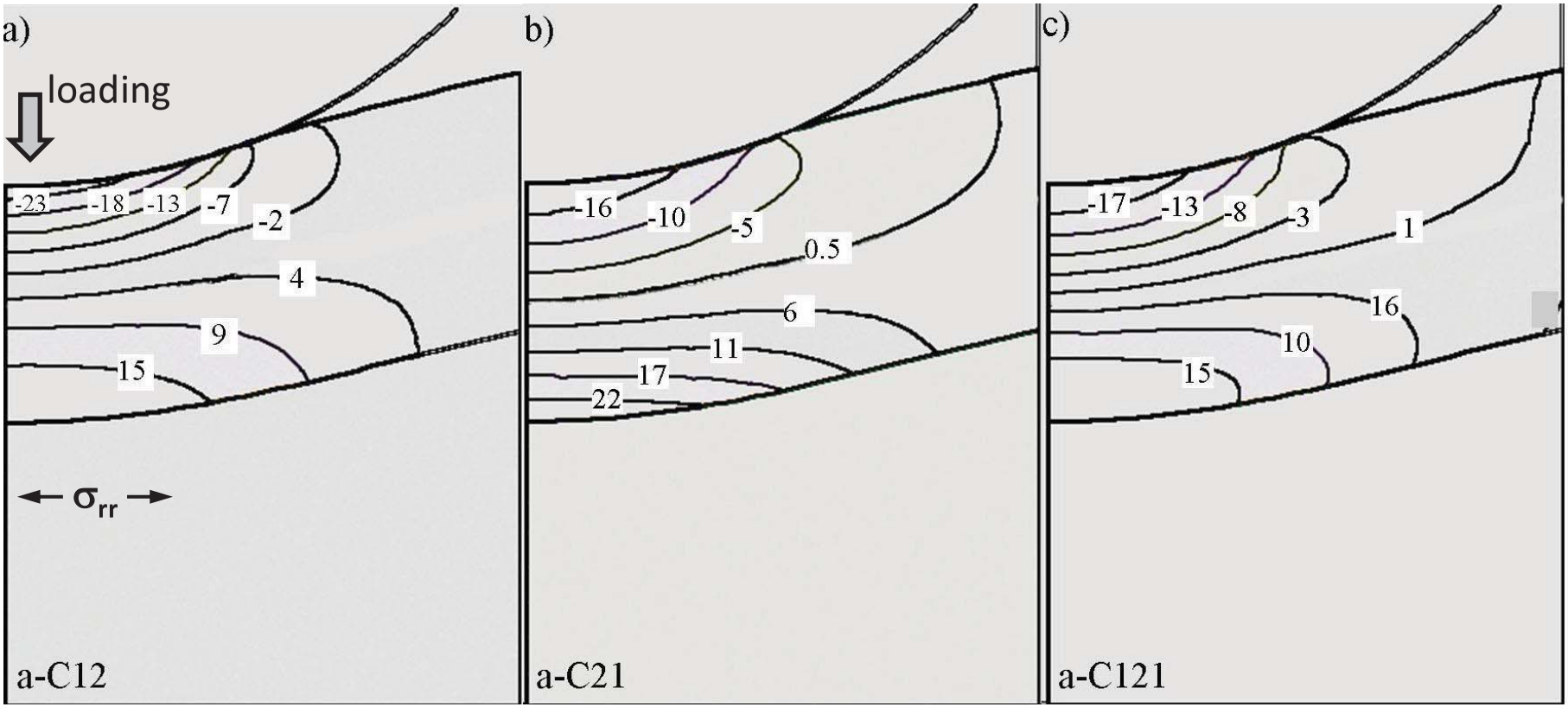

Figure 9
Click here to download Figures (if any): Figure 9.pptx

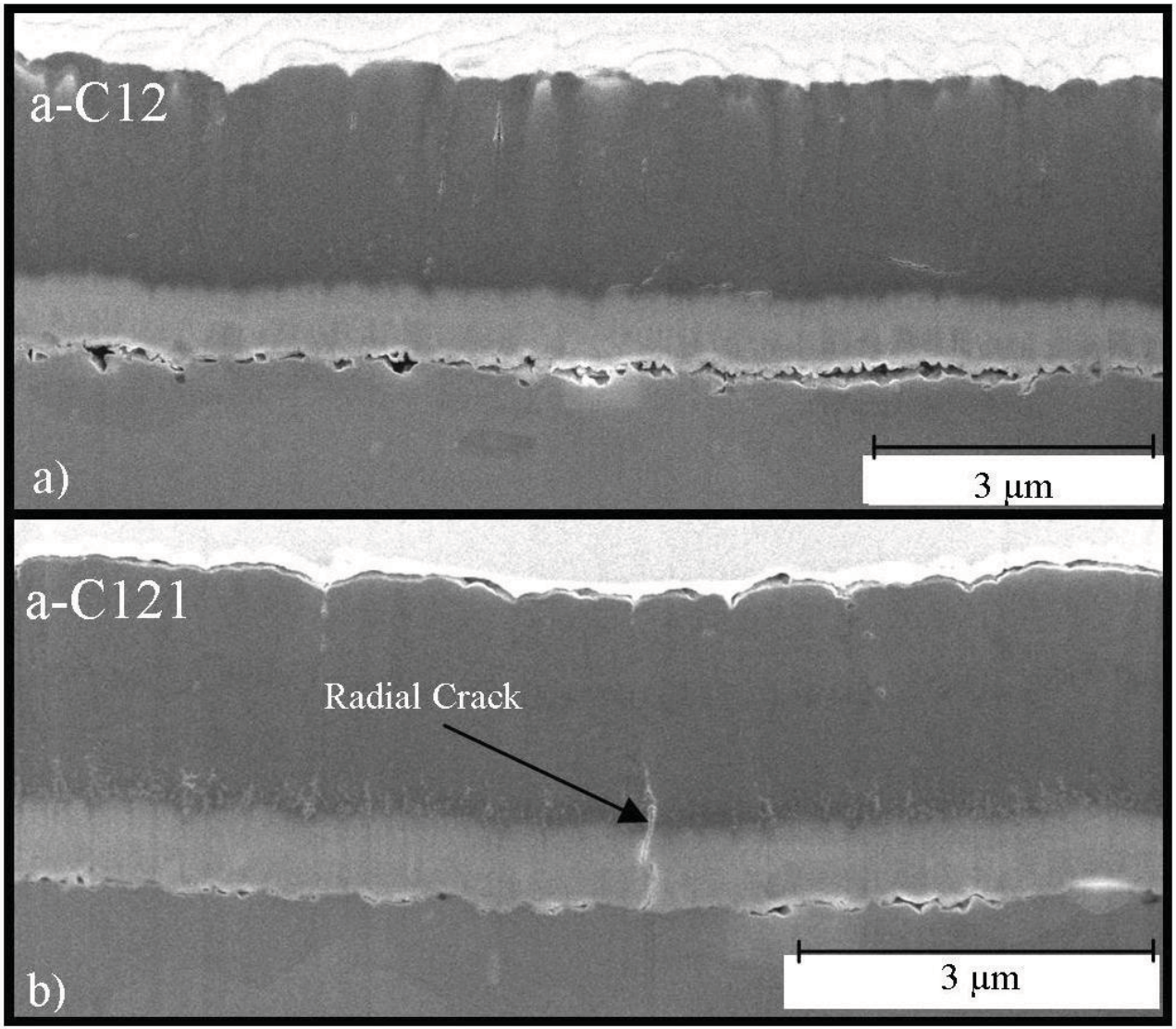

Figure 10
Click here to download Figures (if any): Figure 10.pptx